Journal of Petroleum Science and Engineering 220 (2023) 111155

Contents lists available at ScienceDirect

Journal of Petroleum Science and Engineering

journal homepage: www.elsevier.com/locate/petrol

Creep microindentation of low-density oil well cement and the implication on radial cracking risk of cement sheath

Zhao Chen [a,b,*], Luca Sorelli [b], Philippe Benard [c]

[a] Institute of Mechanics, Chinese Academy of Sciences, Beijing, 100190, China
[b] Department of Civil Engineering, Université Laval, Pavillon Adrien-Pouliot, G1V 0A6, Canada
[c] Holcim Innovation Center, 95 Rue du Montmurier B.P. 15, 38291 Saint Quentin Fallavier Cedex, France

ARTICLE INFO

Keywords:
Low slurry density
Oil well cement
Microindentation
Basic creep
Radial cracking

ABSTRACT

To better provide zonal isolation for the production of oil and gas, low-density oil well cement (LD-OWC) filling a deep oil well was developed to reduce the high hydrostatic pressure caused by the cement slurry. The key mechanical properties of LD-OWC and related cracking susceptibility, nevertheless, have not been fully understood. This work was to characterize the elastic and creep properties of LD-OWC using microindentation and assess the radial cracking risk of the cement sheath. With two types of LD-OWC cured at different temperatures, our measurement through mercury intrusion porosimetry (MIP) showed that their porosities depended on the slurry densities level, and the basic creep exhibited a logarithmic increase in the long term. Mechanical properties such as Young's modulus (E), indentation hardness (H), and creep modulus (C) of LD-OWC were statistically characterized, in particular, E and C were in line with those obtained by macroscopic tests. Moreover, a viscoelastic sheath model was developed to evaluate the stress redistribution in the steel casing, the cement sheath, and the formation in the long term. We found that lower slurry densities of OWC reduced the risk of radial cracking. Taking advantage of parametric analysis, the power-function correlation between the safety factor of radial cracking and the mechanical and geometrical sheath properties was also demonstrated.

1. Introduction

The main objective of well cementing is to provide complete and permanent isolation of the permeable zones located behind the casing in the short and long term (Nelson, E.B., 1990). The number of oil wells is increasing worldwide every year. According to a previous investigation on over 38,000 oil wells globally, the percentage of regional well barrier or integrity failure ranges from 1.9% to 75%. For instance, 43% of 15, 500 offshore wells located in the Gulf of Mexico, USA have experienced failure (Davies et al., 2014). The cement sheath between the steel casing and the formation plays a major role in the zonal isolation (Nelson, E.B., 1990) and is susceptible to different types of failures, e.g., debonding, shear, and radial cracking (De Andrade and Sangesland, 2016). Moreover, high pressure conditions in a deep oil well cement (OWC) sheath may increase the radial cracking risk of the sheath due to the greater tangential tensile stress (Dong et al., 2019).

In general, the OWC employed for a deep well has a slurry density of 1.88 g/cm^3 (or 15.8 ppg) which generates a high hydrostatic pressure against the surrounding formation (Cheng et al., 2018). This pressure is estimated to reach up to 36.8 MPa for a well with a depth of 2 km, which can cause cracking leakage in weak formations. To reduce the slurry density to a lower level of 1.4–1.7 g/cm^3 (12–14 ppg), a minor portion of the clay bentonite is added in the OWC (Cheng et al., 2018; Sha et al., 2018). This increases water-adsorption and requires a high water-to-cement ratio (w/c), which in turn increases the cement porosity and can reduce its strength (Mehta and Monteiro, 2006).

The microstructure of calcium-silicate-hydrate (C–S–H) gel, which governs the strength and the dimensional stability of cement-based materials may undergo structural changes at high temperatures (Alizadeh et al., 2010; Jennings, 2004, 2008; Mehta and Monteiro, 2006). As the temperature of deep wells can reach up to 100–250 °C, the cement phases can transform into other phases, e.g., tobermorite, xonotlite, etc. (Taylor, 1997). Nelson (1990) has elaborated in detail the evolution of cement microstructures at different curing temperatures: (1) at a curing temperature up to 40 °C, the microstructures of unreacted cement particles as well as various hydrates such as C–S–H, calcium hydroxide (CH), ettringite (AFt), and the monosulfoaluminate (AFm) are presented; (2) at atemperature above 60 °C, C–S–H and CH are still the

* Corresponding author. Institute of Mechanics, Chinese Academy of Sciences, Beijing, 100190, China.
E-mail address: zhao.chen.2@ulaval.ca (Z. Chen).

https://doi.org/10.1016/j.petrol.2022.111155
Received 14 January 2022; Received in revised form 11 October 2022; Accepted 22 October 2022
Available online 28 October 2022

major phases, while AFt is unstable and decomposed to AFm; (3) at a curing temperature above 80 °C, C_3AH_6 is formed; (4) at a temperature higher than 110 °C, C–S–H transforms into a dense and crystalline α-C_2SH with formation of surrounding porosity which is detrimental for compressive strength. In practice, the transformation to α-C_2SH can be prevented by adding 35–45% silica, which favors the transformation of C–S–H into a stable microstructure called tobermorite. Moreover, a previous study showed that the elastic modulus of cement paste decreased by 20% when the curing temperature was increased from 20 °C to 60 °C (Valenza II and Thomas, 2012). Another work showed that the creep modulus of class G cement paste decreased (i.e., the increase of creep strain) when the curing temperature was elevated from 60 °C to 90 °C (Vu et al., 2012b).

Cement paste can be effectively modeled from the nanoscale to the macroscale which includes the heterogeneous microstructure, the different length scales of gel, the porous system, and the presence of stiffening inclusions (Pichler and Hellmich, 2011). For instance, nanoindentation can be used to characterize the mechanical properties of cement-based materials for the microstructure phases (Chen et al., 2010; Sorelli et al., 2008; Vandamme and Ulm, 2013). Recently, the microstructure phases of a class G oil well cement (e.g. C–S–H, CH, and AFt) were characterized by coupling nanoindentation techniques and the scanning electron microscopy-energy dispersive X-ray spectrometry (SEM-EDS) (Krakowiak et al., 2015).

Several models have been developed based on the finite element method (FEM) or analytical approach to evaluate the safety of the cement sheath and assure zonal isolation. The analytical methods were mainly based on the plane strain problem of elastic mechanics which applied Lamé solution for a thick cylinder (Gholami et al., 2016; Honglin et al., 2015; Wang et al., 2015). In addition, Wang et al. (2015) employed the elastic-viscoelastic correspondence principle to model the elastic cement sheath surrounded by a viscoelastic salt formation. Moreover, advanced fracture chemo-mechanical models were developed to consider the cement hydration at an early age and the brittle behavior of a cement paste for assessing the radial cracking risk of OWC sheaths (Ardakani and Ulm, 2014; Petersen and Ulm, 2016; Ulm et al., 2014). Furthermore, the 2-D and 3-D FEM models were employed to simulate the sheath structure under thermo-mechanical conditions (De Andrade and Sangesland, 2016; Gholami et al., 2016; Wang and Taleghani, 2014; Wu et al., 2020; Xi et al., 2020; Yan et al., 2020). However, the long-term basic creep of well cement is not included in the aforementioned models, which may be beneficial in relaxing the stress build-up in the sheath. For instance, Brandão et al. (2017) utilized a short-term aging creep model for OWC confirming that the stress of the cement sheath may be significantly overestimated if the viscoelastic properties of the cement sheath were not considered. Moreover, creep is particularly important for LD-OWC which exhibits more creep than normal cement paste due to its higher porosity (Sanahuja and Dormieux, 2010).

Concrete creep is mainly resulted from the viscous behavior of the cement paste which depends on several parameters such as mix design formulations, geometry, temperature, humidity changes, etc.(Neville et al., 1983). The Microprestress-solidification (MPS) theory is a well-established model for concrete creep, which couples Kelvin-Voigt chains for the short-term aging creep and flow module for the long-term basic creep (Bazant et al., 1997). It is generally recognized that the long-term creep of the concrete is logarithmic with no asymptote (Bazant et al., 2011; Brooks and Neville, 1978; Neville et al., 1983; Zhang et al., 2014). Meanwhile, the logarithmic creep compliance function is also applied for the basic creep in the *fib* model code 2010 (Torrenti et al., 2014; Torrenti and Le Roy, 2015).

In the last decade, the indentation technique has emerged as a useful mean to characterize cement paste properties, such as the indentation modulus and the indentation hardness (Oliver and Pharr, 1992, 2004). In particular, microindentation has been frequently employed to investigate the homogeneous properties of the cement paste (Chen et al., 2017, 2020; Chen and Sorelli, 2021; Constantinides and Ulm, 2007; Frech-Baronet et al., 2017; Nguyen et al., 2014). Importantly, Zhang and Vandamme showed that the contact creep modulus (which describes the asymptotic logarithmic creep rate) characterized by a microindentation test in a few minutes correlates well to that measured by compression creep on cement paste and concrete over several years (Zhang et al., 2014).

To the knowledge of the authors, the microindentation study on the LD-OWC system was rarely reported. As the effect of logarithmic basic creep on the long-term integrity of cement sheath is still unknown and requires further investigation, the present work aims at characterizing the mechanical and porous properties of LD-OWC systems using microindentation and mercury intrusion porosimetry (MIP), respectively, emphasizing on their basic creep behavior. Based on the elastic-viscoelastic correspondence principle, a viscoelastic sheath model is developed to evaluate the impact of basic creep on the stress redistribution of the sheath structure. In addition, a parametric analysis is carried out to estimate the safety factor (SF) in a simplified scenario of long-term sheath operation.

2. Materials and methods

2.1. Materials preparation

For this study, we employed a formulation of LD-OWC composed of 96% Class G and 4% bentonite. The addition of bentonite played a role in water-adsorption to reduce the slurry density. Two types of samples with low slurry densities 1.44 g/cm^3 (sample LD_1) and 1.68 g/cm^3 (sample LD_2) were prepared as shown in Table 1. The slurry density of 1.44 g/cm^3 corresponded to a water-binder ratio (w/b) of 1.23, and the slurry density of 1.68 g/cm^3 corresponded to a water-binder ratio (w/b) of 0.68. The samples were then cured in water for 2 months at 38 °C or 82 °C under ambient pressure. Afterward, they were kept in water at 20 °C for 3 months. Cylindrical samples with a diameter of 25 mm and a height of 203 mm were cast and demolded. The cylinders were initially cut off 50 mm from the top and the bottom and were then divided into three parts equal in length. The sample surface was polished before the microindentation testing. A two-step polishing protocol was described as follows: (1) coarse grinding on a rotating equipment with sandpaper of different grit sizes (240, 600, and 1200) until the surface was leveled; (2) Further polishing with an oil-based diamond suspension of two sizes (6 μm and 1 μm).

2.2. Microindentation testing

Microindentation tests were performed on an Anton Paar microindentation tester (MHT) as shown in Fig. 1 (a). A Berkovich tip with an equivalent cone semi-angle of 70.3° was employed. Before the experiment, the tip was calibrated on a certified glass BK-7 with Young's modulus of 83.1 ± 0.4 GPa and a Poisson's ratio of 0.19. The calibrated contact area A_C which is in the function of the contact depth h_c was fitted by using the polynomial function of $A_C(h_c) = C_0h_c^2 + C_1h_c + C_2h_c^{1/2} + C_3h_c^{1/4} + \cdots$, where C_i are the fitting parameters (Oliver and Pharr, 1992). The LD-OWC samples were cured for 24 h at a laboratory relative humidity (RH) of 30% before each test. A grid of 10 × 10 (total 100) matrix microindentation tests were respectively performed on samples $LD_1$38C, $LD_1$82C, $LD_2$38C, and $LD_2$82C. A microscopic indentation

Table 1
Samples of the LD-OWC prepared in this study.

Sample Name	$LD_1$38C	$LD_1$82C	$LD_2$38C	$LD_2$82C
g/cm3	1.44	1.44	1.68	1.68
w/b	1.23	1.23	0.68	0.68
Curing temperature	38 °C	82 °C	38 °C	82 °C

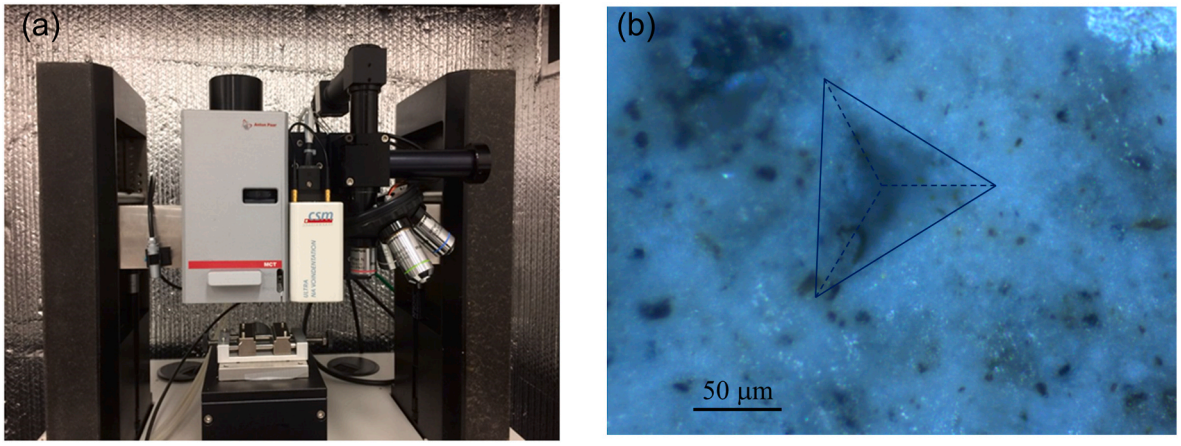

Fig. 1. (a) The microindentation instrument used for this study and (b) an example of microscopic indentation imprint on the sample $LD_2$38C.

residue on LD-OWC was shown in Fig. 1 (b) as an example. To avoid interaction with the neighboring indentation, the inter-distance was set to a value of ten times the indentation depth. Firstly, adjust depth offset (ADO) was carried out to locate the position of the testing surface. Then the tip approached the sample with a slow speed of 16,600 nm/min until it contacted the surface of the sample. Once the initial contact load reached 10 mN, the indenter tip started to penetrate the sample with a loading rate of 24,000 mN/min. At the time slot of 5 s (τ_L), the maximum load of 2 N was reached and was then kept for 300 s (τ_H) to obtain the creep response. Finally, the instrument retracted the tip in 5 s (τ_U) with an unloading rate of 24,000 mN/min.

2.3. Basis of microindentation

The indentation technique is based on the physical principle that the initial unloading is elastic and is not affected by the plasticity induced from the loading phase. The relationship between reduced modulus E_r and the initial slope of the unloading curve S is derived according to the following equation (Oliver and Pharr, 2004)

$$E_r = \frac{S}{2\beta a_u} \tag{1}$$

where β is a factor of 1.034 anda_u is the contact radius between the indenter tip and the indented material at the onset of the unloading phase.

In addition, the relationship between Young's modulus E and the reduced modulus E_r of the indented material is written as

$$\frac{1-\upsilon^2}{E} = \frac{1}{E_r} - \frac{1-\upsilon_i^2}{E_i} \tag{2}$$

where υ is the Poisson's ratio of the specimen; E_i is Young's modulus of the indenter tip; υ_i is the Poisson's ratio of the indenter tip.

The indentation hardness (H) which is empirically related to the materials' strength (Tabor, 2000), is defined as

$$H = \frac{P_{\max}}{A_C} \tag{3}$$

For the indentation with such a sharp Berkovich tip, plasticity is usually generated during the loading phase. To extract the plasticity-independent creep properties through indentation testing, the following equation considering logarithmic creep compliance is employed (Chen et al., 2017)

$$J(t) - J(0) = \frac{2a_u \Delta h(t)}{(1-\nu^2)P_{\max}} = \frac{1}{C}\ln\left(1+\frac{t}{\tau}\right) \tag{4}$$

where $J(t) - J(0)$ is the shifted creep compliance; $\Delta h(t) = h(t) - h(\tau_L)$ is the shifted penetration depth that is equal to the deduction of the depth at the end of the loading phase from the total depth; C is the creep modulus controlling the long-term creep rate; τ is the characteristic time required for the creep curve to reach the logarithmic response.

3. Results

3.1. Mercury intrusion porosimetry

The porosities of LD-OWC samples were measured using the mercury intrusion porosimetry (MIP) technique. A fragment of about 1 g was cut out from each sample and was then dried using the solvent exchange method to remove the pore water as previously reported (Scrivener et al., 2016). The fragments were kept in isopropanol for 7 days with daily changes of the solvent and were then kept in a desiccator for 7 days to remove the isopropanol residual. As shown in Table 2, elevating the curing temperature from 38 °C to 82 °C slightly increased the porosity by 3% for both LD_1 and LD_2 systems. At the same curing temperature, the porosity of the LD_2 system is 17% lower than that of the LD_1 system. As shown in Fig. 2 (a), pores with a size of 2–30 nm were generated more in the samples cured at a higher temperature of 82 °C. The critical pore entry radius (CPER) which corresponded to the peak of the pore distribution curves, as plotted in Fig. 2 (b), had a decreasing shift when the curing temperature was elevated. Specifically, the CPER for LD_1 was decreased from 176 nm to 132 nm, and the CPER for LD_2 was decreased from 43 nm to 35 nm when the curing temperature was increased from 38 °C to 82 °C.

3.2. Microindentation results

The mean microindentation curves of penetration load versus penetration depth were plotted in Fig. 3 (a), which were in turn divided into three parts: a polynomial loading curve, a slow creep penetration line under a constant load, and a quick unloading curve. It showed that the sample LD_2 had a lower maximum indentation depth compared to the sample LD_1, while samples cured at 82 °C displayed a larger indentation depth than those cured at 38 °C. Furthermore, the mean shifted curves of microindentation creep were plotted and compared in Fig. 3 (b). As shown in this semi-log plot, the creep curves were linearly proportional to the logarithmic time after several seconds. Moreover, the LD_1 system exhibited a higher creep response compared with the LD_2

Table 2
Porosities of LD-OWC samples.

Sample Name	$LD_1$38C	$LD_1$82C	$LD_2$38C	$LD_2$82C
Porosity (%)	57	60	40	43

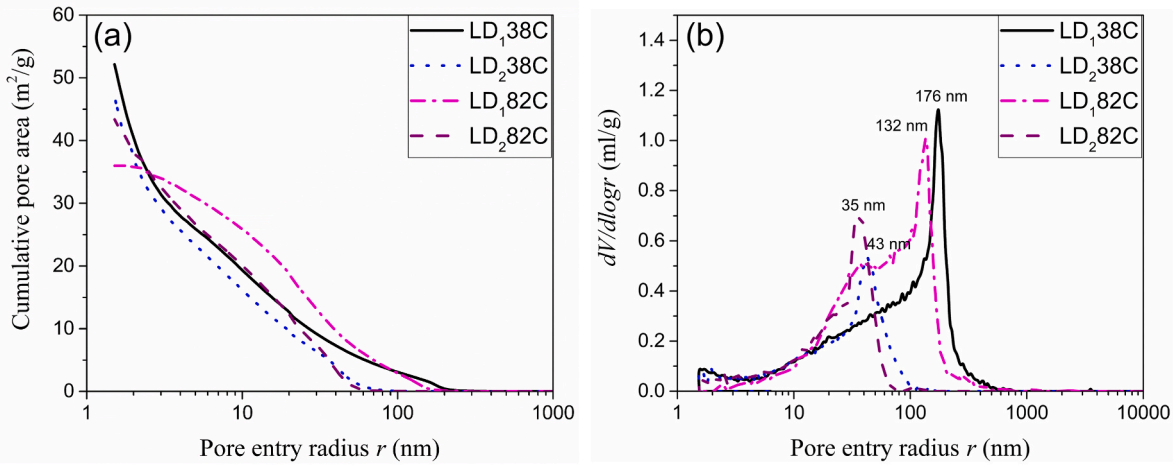

Fig. 2. Plots of (a) cumulative pore area versus pore entry radius and (b) first derivatives of the cumulative curves.

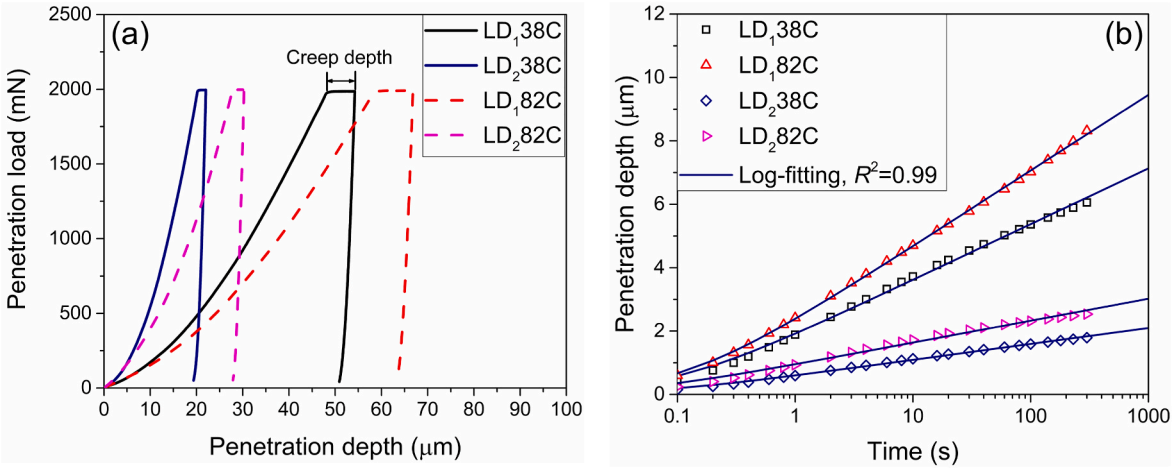

Fig. 3. (a) Mean experimental curves of penetration load versus penetration depth; (b) mean experimental data (symbol) of microindentation creep fitted by logarithmic creep compliance (solid line).

system due to its higher porosity as summarized in Table 2. Clearly, samples cured at the higher temperature 82 °C showed more creep than the samples cured at 38 °C. Each creep curve was well fitted by the logarithmic creep compliance of Eq. (4) with a coefficient of determination (R^2) of 0.99.

The microindentation testing results were summarized in Table 3 in the form of average ± standard deviation. Generally, mean values of *H*, *E*, and *C* of LD_1 and LD_2 were reduced when the curing temperature was increased to 82 °C. For example for the LD_1 system, the indentation hardness H was reduced from 29.9 MPa to 19.2 MPa; the indentation modulus *E* was decreased from 3.1 GPa to 2.3 GPa; the creep modulus *C* was decreased from 9.7 GPa to 5.0 GPa. A similar decreasing trend of microindentation results (*H*, *E*, and *C*) was observed for the LD_2 system when the curing temperature was increased. By comparing the LD_1 and LD_2 systems, *H*, *E*, and *C* were greatly enhanced for the LD_2 system due to a lower *w/b* ratio of 0.68. The experimental values of *H*, *E*, and *C* were presented with a 3-D plot in Fig. 4, which clearly showed the shift of the data clusters due to different curing temperatures and slurry densities. The lower the *w/b* was, the higher the values of *H*, *E*, and *C* were. Whereas, the higher the curing temperature was, the lower the values of *H*, *E*, and *C* were. In addition, the normal distribution curves plotted over the histograms were shown in Fig. 5. Similar effects of *w/b* and curing temperature on the mechanical properties (*H*, *E*, and *C*) could be observed, which were higher at a lower ratio *w/b* and lower at a higher temperature.

Table 3
Microindentation properties (H, E, and C) of the studied OWC systems.

Sample	*H* (MPa)	*E* (GPa)	*C* (GPa)
$LD_1$38C	29.9 ± 8.2	3.1 ± 0.4	9.7 ± 2.5
$LD_1$82C	19.2 ± 3.3	2.3 ± 0.2	5.0 ± 1.0
$LD_2$38C	187.4 ± 58.5	10.1 ± 1.6	85.8 ± 23.2
$LD_2$82C	95.1 ± 11.3	7.0 ± 0.3	47.9 ± 5.2

3.3. Statistical analysis

As shown in Table 3, the mean values of *E*, *H*, and *C* were significantly enhanced by increasing *w/b* and decreased by increasing the curing temperature. To further confirm if the interplay between *w/b* and curing temperature also affected *E*, *H*, and *C*, a two-way analysis of variance (ANOVA) was adopted. As shown in Table 4, all *F*-values of the Fisher-Snedecor distribution were far greater than the critical *F*-values ($F \gg F_{crit} = 3.9$). *P*-values corresponding to normal distribution were far below the significance level $\alpha = 0.05$ ($P \ll 0.05$). For the factor of *w/b*, it is notable that *F*-values were considerably large and *P*-values were extremely low. These results were reasonable as there were obvious differences in the mean values of *E*, *H*, and *C* at two levels of *w/b*, which strongly deviated from the equal means of the null hypothesis. For

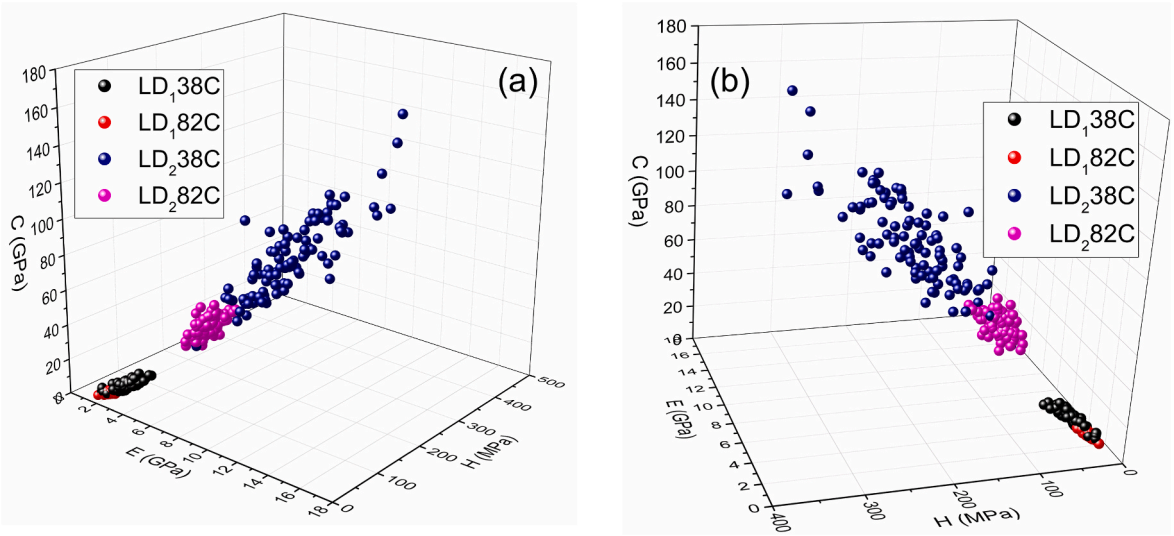

Fig. 4. A 3-D plot of data clusters for E, H, and C.

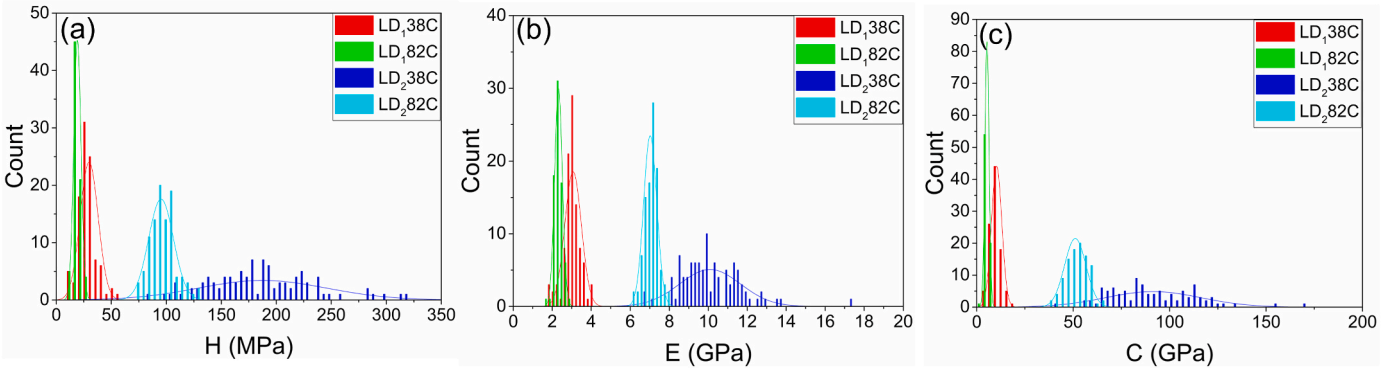

Fig. 5. Histogram distributions of (a) indentation hardness (H); (b) Young's modulus (E); (c) creep modulus (C).

Table 4
ANOVA of E, H, and C with two factors of curing temperature and water-binder ratio (w/b) at the significance level $\alpha = 0.05$.

Factors	*E*		*H*		*C*		
	P	F	P	F	P	F	F_{crit}
Curing temperature	8.3×10^{-58}	409.9	7.6×10^{-37}	214.0	1.8×10^{-39}	235.2	3.9
Water-binder ratio	6.7×10^{-166}	3492.4	2.3×10^{-98}	1029.6	4.4×10^{-124}	1681.1	3.9
Interaction	1.9×10^{-29}	158.9	2.3×10^{-27}	144.4	1.0×10^{-28}	153.8	3.9

instance, *E*, *H*, and *C* values of $LD_2$38C system were 3.3, 6.3, and 8.8 times of $LD_1$38C system, respectively. We can thus conclude that the effects of curing temperature and *w/b* on *E*, *H*, and *C* are statistically significant. Furthermore, it can be confirmed that there was a cross-over interaction between the two factors indicating that the effects of curing temperature and *w/b* on the mechanical properties of the LD-OWC system were related.

3.4. Comparison of Young's modulus (E) and creep modulus (C) with previous works

The indenter tip penetrates the LD-OWC samples with the depth ranging from 20 μm to 60 μm in this study. Within this scale, the sample normally contains sufficient microstructures such as the C–S–H, the CH, the clinker, capillary pores, etc., represents a type of mechanically homogeneous material (Chen et al., 2017; Chen and Sorelli, 2021; Frech-Baronet et al., 2017; Zhang et al., 2014). To apply the microindentation results at the engineering scale, we compared values of Young's modulus *E* with those obtained by macroscopic tests, such as uniaxial compressive tests on class G cement (Vu et al., 2012a) and beam bending tests on ordinary Portland cement (OPC) (Valenza II and Thomas, 2012). Briefly, the samples of class G cement paste were cured at 60 °C and 90 °C for three months before the experiment, while the OPC specimens were cured at 40 °C and 60 °C respectively(Vu et al., 2012a) (Valenza II and Thomas, 2012). As shown in Fig. 6 (a), greater curing temperatures decreased Young's modulus for all the tests. Owing to the greater *w/c* ratio, the *E* value of LD_2 (*w/b* = 0.68) cured at 38 °C was lower than that of class G cement (*w/c* = 0.44) cured at 60 °C and that of the OPC (*w/c* = 0.45) cured at 40 °C. And this was verified in Fig. 6 (b) demonstrating the effects of *w/b* (*w/c*) on Young's modulus measured by microindentation in this work compared with those measured on conventional class G cement (with different *w/b* of 0.4, 0.5, 0.6, and 0.8) cured at 25–29 °C (Guner et al., 2017), in which a similar decreasing tendency of *E* with the increase of *w/b* ratio was found and

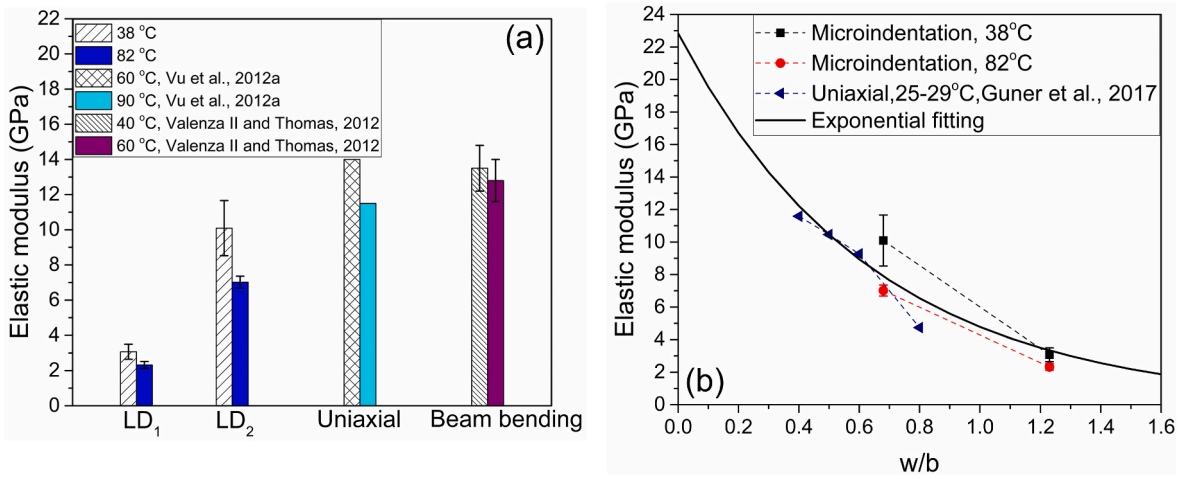

Fig. 6. Comparison of the microindentation results with previous studies for (a) the effect of curing temperature on Young's modulus of LD-OWC and (b) the relationship between Young's modulus and w/b (or w/c).

could be fitted by an empirically exponential function: $E(w/b) = \alpha e^{-\beta(w/b)}$ ($\alpha = 22.8$; $\beta = 1.6$, R^2 of 0.85).

It has been recently demonstrated that the creep modulus of cement paste generated in minutes-long microindentation correlates well with that measured by macroscopic uniaxial experiments lasting 5 years (Zhang et al., 2014). To verify this relation, we compared the creep modulus C obtained using microindentation tests with the C analyzed from the uniaxial compressive experiment. Notably, Vu et al. (2012b) carried out a uniaxial compression creep experiment on the class G cement paste ($w/c = 0.44$) considering two curing temperatures of 60 °C and 90 °C. First of all, Fig. 7 shows the modeling of Vu et al.'s results with a logarithmic creep compliance function which was employed in the microindentation study of Eq. (4), i.e., $J(t) - J(0) = \ln(1 + t/\tau)/C$ with a coefficient of $R^2 = 0.99$. In detail, at a curing temperature of 60 °C and a compressive pressure of 20 MPa, C and τ were 131.2 GPa and 8.4 h respectively. At 90 °C and 20 MPa, C and τ were 85.1 GPa and 4.9 h. At 90 °C and 25 MPa, C and τ were 66.9 GPa and 6.0 h, respectively. Furthermore, the creep modulus C of class G cement paste was compared with that of LD-OWC samples measured in this work in Fig. 8. The results are in agreement which showed that increasing the curing temperature decreased the creep modulus and thus increased the creep deformation.

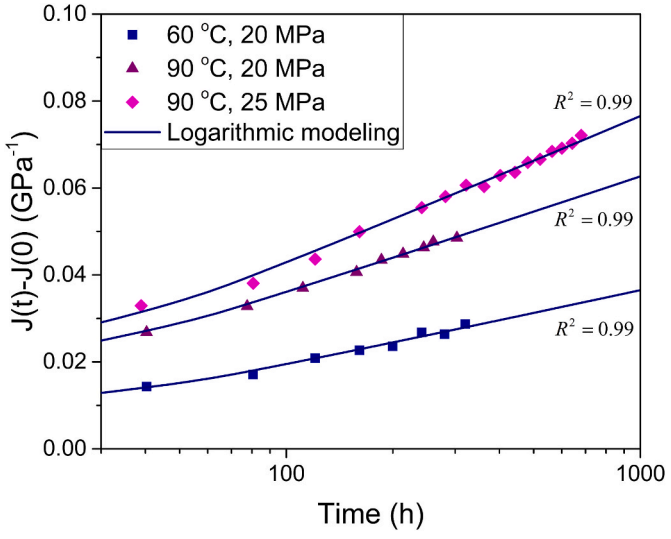

Fig. 7. Logarithmic modeling of the uniaxial compression creep results of Vu et al. (2012b) on conventional class G cement (w/c = 0.44) in semi-log time scale.

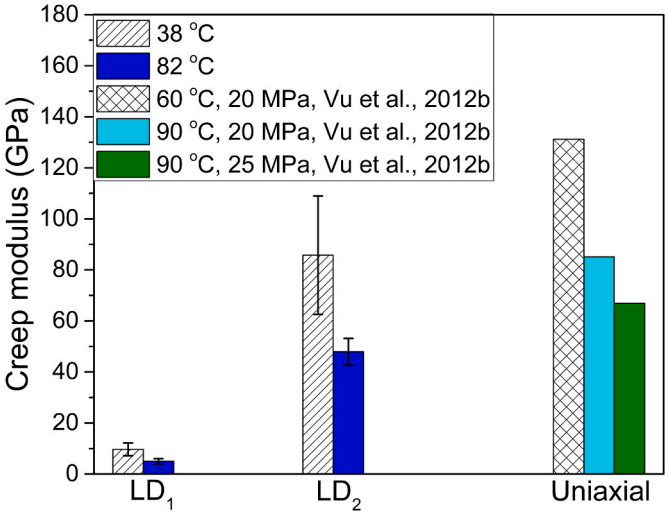

Fig. 8. Comparison of the creep modulus (C) of LD-OWC measured by microindentation in this work and the C of class G cement paste through uniaxial creep experiment.

Compared with the uniaxial results, the lower creep modulus of the LD-OWC sample was due to the higher values of the w/b ratio.

4. Safety assessment of the cement sheath

Considering the viscoelastic behavior of a cement paste is essential to estimate the stress build-up in LD-OWC sheaths in the long term, a first-order viscoelastic model was developed to assess the mechanical behavior of LD-OWC.

4.1. Viscoelastic modeling of the sheath structure

For the mechanical modeling, we considered a linear loading and a constant holding under internal pressure p_i and external pressure p_e (Fig. 9 (a)) which may represent the initial pumping or the pumping operation after a possible interruption, which occurs frequently in oil production. To simplify the process, we assumed a linear increase of p_i and p_e during a certain loading time t_L for the initial or reactivated pumping and a constant holding of p_i and p_e for a subsequent duration t_H indicating the restoration of oil production (Fig. 9 (b)). The temperature was considered constant which indicated that there was no temperature-

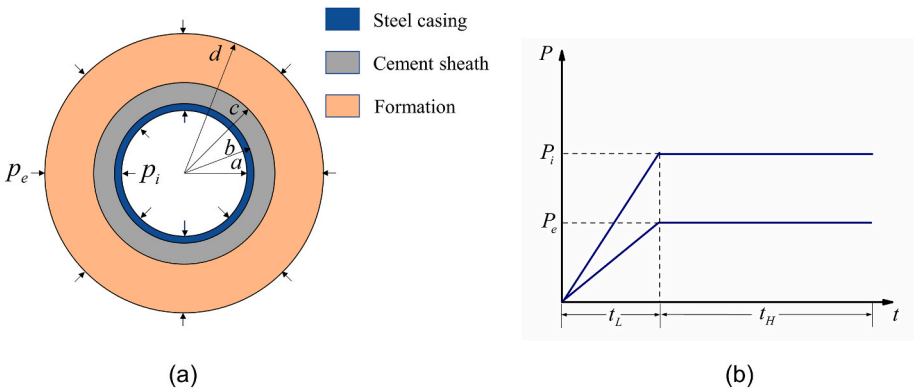

Fig. 9. (a) Schematic view of a sheath structure subjected to internal and external pressure; (b) loading history for internal and external pressure.

induced stress in the sheath structure.

The sheath structure in the longitudinal direction (or z-direction) far exceeded its transversal direction. Moreover, the internal pressure p_i and the external pressurep_e were applied in the direction perpendicular to the z-direction. Under these conditions, the elasticity of the well sheath structure can be understood as a plane strain problem (Timoshenko and Goodier, 1951). As shown in Fig. 10, the sheath structure consisted of three layers of hollow cylinders: steel casing ($r = a \sim b$), cement sheath ($r = b \sim c$), and formation ($r = c \sim d$). The basic assumption was that the deformation of the cement sheath was viscoelastic, and the deformation of the steel casing and the formation was elastic. Each separated cylinder was subjected to the distributed pressure shown in Fig. 10. p_i and p_e were the pressure acting on the internal steel casing and the external formation, respectively. p_1 and p_2 were the interface pressure between the steel casing and the cement sheath, and the pressure between the cement sheath and the formation, respectively. Besides, the displacement between the steel casing and the cement sheath, and the displacement between the cement sheath and the formation met the continuity conditions.

Notably, the time-dependent viscoelasticity problem can be transformed into the elastic problem within the Laplace-Carson domain when the correspondence principle was applied. After inverting the Laplace operator of the elastic solution, one can subsequently obtain the time-dependent stress or strain response (Lee and Radok, 1960). In the following analysis, we referred to an elastic scheme that has been validated by FEM (Honglin et al., 2015). The upper star * denotes the terms of the Laplace-Carson operators, i.e., $F^* = s\int_0^\infty e^{-st}f(t)dt$, which can be inverted to the time domain by $f(t) = L^{-1}(F^*/s)$. In the Laplace-Carson domain, the mathematical expressions of the internal and external pressure were written as

$$p_i^* = \frac{(1-e^{-st_L})p_i}{st_L}, p_e^* = \frac{(1-e^{-st_L})p_e}{st_L} \tag{5}$$

Besides, the creep compliance of Eq. (4) in the Laplace-Carson domain was given by (Chen et al., 2017)

$$J^* = \frac{1}{E} + \frac{e^{\tau s}Ei(\tau s)}{C} \tag{6}$$

where the term $Ei(\tau s)$ indicated the exponential integral function of τs. Through the correlated relationship between the creep compliance and the relaxation modulus ($E^* = 1/J^*$), the relaxation modulus can be written as

$$E^* = \frac{EC}{C + e^{\tau s}Ei(\tau s)E} \tag{7}$$

Then, equations of Hook's law in the Laplace-Carson domain were written as

$$\begin{aligned} \varepsilon_r^* &= \frac{1}{E^*}\left[\sigma_r^* - \nu(\sigma_\theta^* + \sigma_z^*)\right] \\ \varepsilon_\theta^* &= \frac{1}{E^*}\left[\sigma_\theta^* - \nu(\sigma_r^* + \sigma_z^*)\right] \\ \gamma_{r\theta}^* &= \frac{\tau_{r\theta}^*}{G} \end{aligned} \tag{8}$$

where Poisson's ratio was assumed as a constant, i.e., $\nu^* = \nu$. According to the plane strain assumption, the relation $\sigma_z^* = \nu(\sigma_r^* + \sigma_\theta^*)$ can be derived from$\varepsilon_z^* = [\sigma_z^* - \nu(\sigma_r^* + \sigma_\theta^*)]/E^* = 0$. Regarding the symmetrical structure subjected to uniformly internal and external stress, the shear stress $\tau_{r\theta}^*$ and the shear strain $\gamma_{r\theta}^*$ must be zero. Consequently, Eq. (8) can be rewritten as

$$\begin{aligned} \varepsilon_r^* &= \frac{1}{E^*}\left[(1-\nu^2)\sigma_r^* - \nu(1+\nu)\sigma_\theta^*\right] \\ \varepsilon_\theta^* &= \frac{1}{E^*}\left[(1-\nu^2)\sigma_\theta^* - \nu(1+\nu)\sigma_r^*\right] \end{aligned} \tag{9}$$

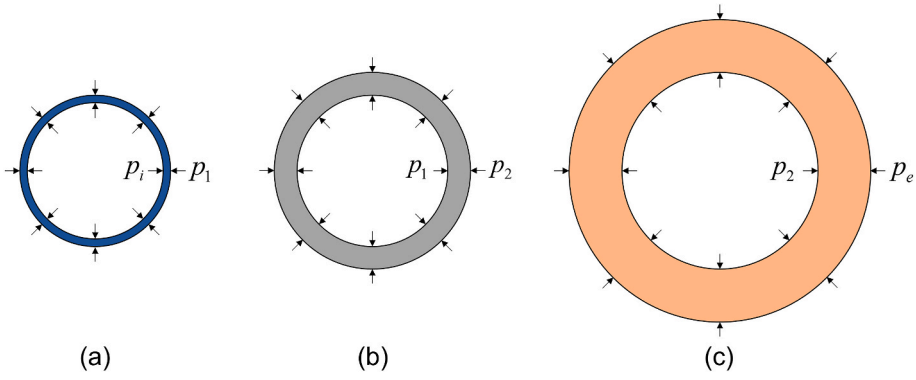

Fig. 10. Internal and external pressure on (a) steel casing, (b) cement sheath, and (c) formation.

After that, the radial displacement was given by

$$u_r^* = r\varepsilon_\theta^* = \frac{r}{E^*}\left[(1-\nu^2)\sigma_\theta^* - \nu(1+\nu)\sigma_r^*\right] \tag{10}$$

Firstly, according to the solution of Lamé problem (Timoshenko and Goodier, 1951), the radial stress σ_{rs} and the tangential stress $\sigma_{\theta s}$ in the steel casing, as shown in Fig. 13 (b), were written as

$$\sigma_{rs}^* = \frac{p_i^* a^2}{b^2-a^2}\left(1-\frac{b^2}{r^2}\right) - \frac{p_1^* b^2}{b^2-a^2}\left(1-\frac{a^2}{r^2}\right) \tag{11}$$

$$\sigma_{\theta s}^* = \frac{p_i^* a^2}{b^2-a^2}\left(1+\frac{b^2}{r^2}\right) - \frac{p_1^* b^2}{b^2-a^2}\left(1+\frac{a^2}{r^2}\right) \tag{12}$$

Combining Eqs. (10)–(12), the radial displacement of the steel casing at $r = b$ was given by

$$u_{rs}^*(r=b) = \frac{b}{E_s}\left[(1-\nu_s^2)\sigma_{\theta s}^* - \nu_s(1+\nu_s)\sigma_{rs}^*\right] \tag{13}$$

Secondly, after applying the Lamé solution to the cement sheath, the radial and the tangential stress were written as

$$\sigma_{rc}^* = \frac{p_1^* b^2}{c^2-b^2}\left(1-\frac{c^2}{r^2}\right) - \frac{p_2^* c^2}{c^2-b^2}\left(1-\frac{b^2}{r^2}\right) \tag{14}$$

$$\sigma_{\theta c}^* = \frac{p_1^* b^2}{c^2-b^2}\left(1+\frac{c^2}{r^2}\right) - \frac{p_2^* c^2}{c^2-b^2}\left(1+\frac{b^2}{r^2}\right) \tag{15}$$

Similarly, the radial displacement of the cement sheath at $r = b$ was given by

$$u_{rc}^*(r=b) = \frac{b}{E^*}\left[(1-\nu_c^2)\sigma_{\theta c}^* - \nu_c(1+\nu_c)\sigma_{rc}^*\right] \tag{16}$$

Thus, the radial displacement of the cement sheath at $r = c$ was written as

$$u_{rc}^*(r=c) = \frac{c}{E^*}\left[(1-\nu_c^2)\sigma_{\theta c}^* - \nu_c(1+\nu_c)\sigma_{rc}^*\right] \tag{17}$$

Thirdly, the radial and the tangential stress of the formation were given by

$$\sigma_{rf}^* = \frac{p_2^* c^2}{d^2-c^2}\left(1-\frac{d^2}{r^2}\right) - \frac{p_e^* d^2}{d^2-c^2}\left(1-\frac{c^2}{r^2}\right) \tag{18}$$

$$\sigma_{\theta f}^* = \frac{p_2^* c^2}{d^2-c^2}\left(1+\frac{d^2}{r^2}\right) - \frac{p_e^* d^2}{d^2-c^2}\left(1+\frac{c^2}{r^2}\right) \tag{19}$$

With Eq. (10), the radial displacement of the cement sheath at $r = c$ read

$$u_{rf}^*(r=c) = \frac{c}{E_f}\left[\left(1-\nu_f^2\right)\sigma_{\theta f}^* - \nu_f\left(1+\nu_f\right)\sigma_{rf}^*\right] \tag{20}$$

Moreover, the radial displacement should meet the continuity conditions at the interface $r = b$ and $r = c$, which was given by

$$u_{rs}^*(r=b) = u_{rc}^*(r=b), u_{rc}^*(r=c) = u_{rf}^*(r=c) \tag{21}$$

Combining Eqs. ((13), (16), (17), (20) and (21) led to the solution of the unknown interface pressure p_1^* and p_2^*, which may, in turn, give the solution of the radial stress and the tangential stress distributed in each cylinder. Because of the exponential integral functions in solutions, radial stress σ_r^* and tangential stress σ_θ^* are in complex forms and cannot be analytically inverted to the time domain. We thus employed a numerical algorithm of the Gaver-Stehfest method (Abate and Whitt, 2006) to obtain the time-dependent $\sigma_r(t)$ and $\sigma_\theta(t)$, which were written as

$$\widehat{f}(t,\overline{M}) = \frac{\ln(2)}{t}\sum_{k=1}^{2\overline{M}}\zeta_k\widehat{f}\left(\frac{k\ln(2)}{t}\right)$$
$$\zeta_k = (-1)^{\overline{M}+k}\sum_{j=\lfloor(k+1)/2\rfloor}^{k\wedge\overline{M}}\frac{j^{\overline{M}+1}}{\overline{M}!}\binom{\overline{M}}{j}\binom{2j}{j}\binom{j}{k-j} \tag{22}$$

where $\overline{M}$ indicated the positive integer controlling the precision, $[(k+1)/2]$ was the greatest integer less than or equal to $(k+1)/2$, and $k \wedge \overline{M} = \min(k, \overline{M})$ was the minimum value of k and $\overline{M}$.

As to the creep modeling parameters, Young's modulus and the creep modulus of LD-OWC shown in Table 3 were employed. Other physical and geometric parameters were summarized in Table 5 which were similar to the values in the previous literature (Honglin et al., 2015; Wang et al., 2015).

The radial and tangential stress of the cement sheath were plotted in Fig. 11 (a) and (b), respectively. Generally, at the loading phase, the stress increased from zero to the maximum value in a nonlinear fashion. Distinguished from the elastic solution, the maximum radial and tangential stress were reached at a time slot slightly later than the time point t_L for the maximum loading. This difference may be explained by the viscoelastic feature of cement sheath. It can be observed that the stress decreases in the long term during the holding phase. In general, the stress level of the LD_2 system was higher than that of LD_1. LD_1 showed more relaxation due to the lower creep modulus which allowed more creep and thus stress relaxation response. The radial and tangential stress of the formation showed a similar trend to that of cement sheath as shown in Fig. 12. The tangential stress of the steel casing, as shown in Fig. 13 (a), nevertheless, was increased due to the shifted stress from the stress relaxation of the cement sheath and the formation. Although the steel material possessed much higher yield strength than cement paste, attention should be paid to the tangential stress of steel casing design to avoid exceeding its yield point.

4.2. Radial cracking risk

Following a previous study (De Andrade and Sangesland, 2016), the safety factor (*SF*) was considered to evaluate the radial cracking of the cement sheath:

$$SF = |TS / \sigma_\theta| \tag{23}$$

where *TS* refers to the tensile strength of the OWC materials. It has been known that the uniaxial compressive strength (*UCS*) was correlated to Young's modulus *E* in cement-based materials. Moreover, the *TS* is far below the *UCS* ($TS \approx 0.1UCS$) due to the intrinsic microstructure of cement material that is prone to cracking. According to a previous study by De Andrade and Sangesland (2016), a quadratic parabolic relationship between *UCS* and *E*, and a linear relationship between *UCS* and *TS*, could be established using published data of various cement systems with *E* ranging from 0.5 GPa to 16.6 GPa. Based on those results, we derived and obtained a similar quadratic parabolic correlation between *TS* and *E* and subsequently fitted it with a power function ($R^2 = 0.999$) for the following parametric analysis, which was written as

$$TS = 0.42E^{1.1} \tag{24}$$

Table 5
Mechanical, loading, and geometric parameters assumed for the analysis.

Mechanical	Value	Loading	Value	Geometric	Value
E_s (GPa)	200	P_i (MPa)	−30	a (mm)	100
ν_s	0.3	P_e (MPa)	−2.9	b (mm)	110
E_f (GPa)	40	t_H (day)	1000	c (mm)	140
ν_f	0.3	t_L (hour)	1	d (mm)	1040
ν_c	0.2	–	–	–	–

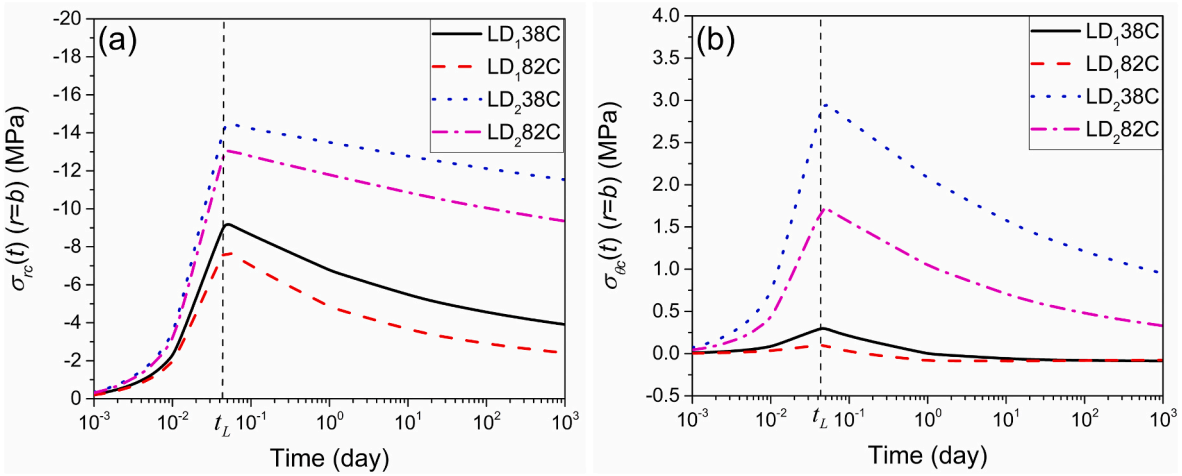

Fig. 11. (a) Radial stress and (b) tangential stress of cement sheath.

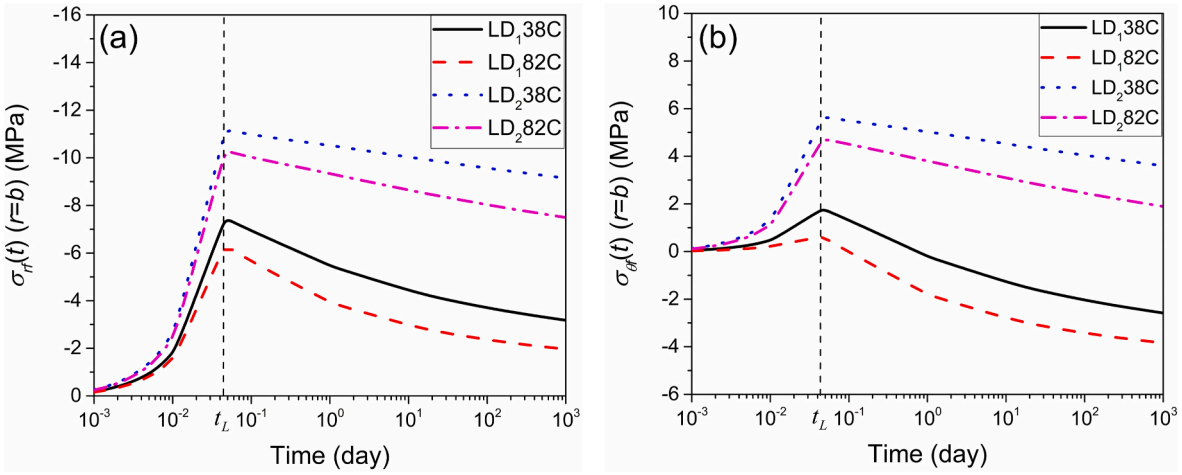

Fig. 12. (a) Radial stress and (b) tangential stress of formation.

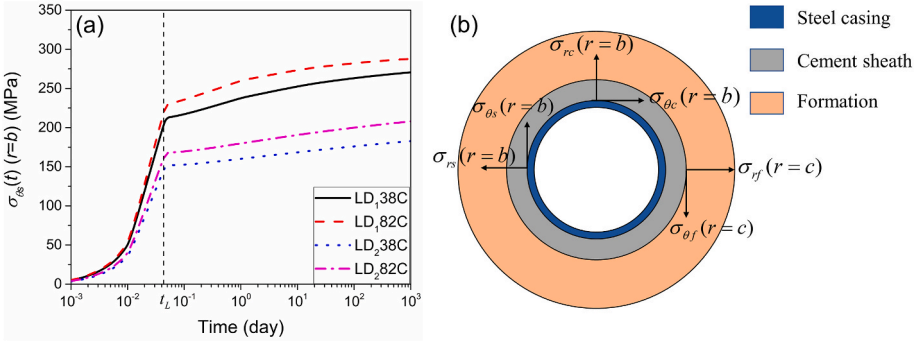

Fig. 13. (a) Tangential stress of steel casing and (b) schematic diagram of radial and tangential stress in the sheath structure.

where the units of *TS* and *E* are MPa and GPa respectively. Details for the derivation of Eq. (24) can be found in Appendix A. Note that this equation was fitted through the experimental results of *TS* and *E* measured at ambient temperature. Thus, the authors only considered the measured *E* of LD-OWC cured at 38 °C for this study which was close to the ambient temperature in the reference.

Combing Eq. (23) and Eq. (24), the evolution of *SF* was plotted in Fig. 14 based on the measured *E* through microindentation tests, and the analysis results of the radial stress σ_θ (Fig. 11). Generally, the *SF* of the studied materials initially decreased during the loading phase and then increased after the time slot t_L at the end of the loading phase, when the minimum *SF* was observed. In other words, the cracking risk was the highest at the end of the loading phase. Besides, at the time point $t = t_L$, the *SF* for the LD_1 sample was 5.1 which is higher than the *SF* for the LD_2 sample ($SF = 1.8$). This means that cement sheath with a lower slurry density (or higher *w/b*) shows a lower radial cracking risk, providing better protection for the well integrity.

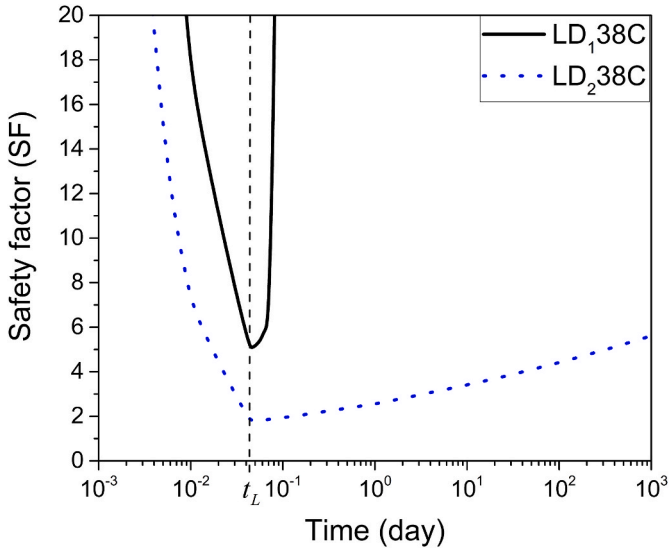

Fig. 14. Time evolution of SF for LD-OWC.

4.3. Parametric analysis and radial cracking susceptibility index

A parametric analysis of the SF was carried out to estimate the effect of the key properties of materials and structures in the long term. In the analytical modeling, the safety factor determining the cracking risk of the cement sheath was mainly affected by the following variables: Young's modulus (E, E_f), the tensile strength (TS), the creep modulus (C) of the cement sheath, the internal pressure (P_i), and the geometric parameters of steel casing and cement sheath (a, b, c). The dimension of formation d was much greater than a, b, c and was not considered as a key factor. It has been shown in Eq. (24) that there was a power relation between TS and E, i.e., $TS = 0.42E^{1.1}$. Moreover, inspired by the work of Vandamme and Ulm (2009), a power function was employed to fit the correlation between C and E in this study. As shown in (a), all the data of C and E for the LD-OWC cured at 38 °C were plotted and fitted with a power function, i.e.$C = 1.84E^{1.65}$. A coefficient of $R^2 = 0.96$ indicated a good correlation between C and E. This confirms that the power function correlation between the C and E which was previously found for ordinary Portland cement also applies to LD-OWC.

Moreover, the influencing parameters E, C, and TS can be reduced to a single parameter E. Then, six parameters were considered for estimating the radial cracking risk of cement sheath: E, E_f, P_i, a, b, c. Based on the modeling scheme developed, 108 analyses were carried out to calculate the minimum SF at the end of the loading phase. The parametric analysis was then performed with the following variable ranges: E (2.5, 5.3, 8.9,13.4 GPa), E_f (10, 30, 60 GPa),P_i (20, 30, 40 MPa), and (a, b, c) [(95, 105, 125), (100, 115, 145), (105, 125, 165) mm]. Finally, dimensional analysis was carried out to express the SF and the radial cracking risk was defined as the product of a series of power functions as follows (Sorelli et al., 2006)

$$SF = \alpha_1 E^{\alpha_2} E_f^{\alpha_3} P_i^{\alpha_4} a^{\alpha_5} b^{\alpha_6} c^{\alpha_7} \tag{25}$$

where α_i (i = 1...7) were exponents to the best fit against the experimental data. As in an empirical equation, the dimensions for α_i were not labeled. Using a method based on least squares, these radial cracking susceptibility indexes were obtained by fitting Eq. (25) with the SF through the analytical modeling ($R^2 = 0.85$) as shown in Fig. 15 (b) with the following exponents: $\alpha_1 = 0.276$, $\alpha_2 = -0.905$, $\alpha_3 = 0.554$ $\alpha_4 = -0.980$, $\alpha_5 = 0.462$, $\alpha_6 = 0.592$, and $\alpha_7 = 0.159$. The analytical SF (Eq. (23)) and the approximated SF (Eq. (25)) were compared and plotted. In general, SF was positively related to the parameters E_f, a, b, c, and was negatively related to the parameters E, P_i. It can thus be concluded that increasing Young's modulus of formation and the geometry dimension can increase the SF and thus lower the radial cracking risk, while increasing Young's modulus of cement sheath and the internal pressure may decrease the SF and thus elevate the radial cracking risk.

5. Conclusions and outlook

Based on the experimental and analytical modeling results, the following conclusions can be drawn from this study:

- Increasing the curing temperature from 38 °C to 82 °C slightly increased the porosity of the LD-OWC system by 3%. At the same curing temperature, the porosity of the lighter LD_1 system was 17% higher than that of the LD_2 system.
- Increasing the curing temperature decreased the mechanical properties of LD-OWC such as the indentation hardness H and Young's modulus E. It also decreased the creep modulus C and therefore enhanced the creep response.
- The mechanical properties of LD-OWC characterized by microindentation agreed with the macroscopic results experimented on class G cement or OPC. Compared with the macroscopic experiment, the creep modulus C can be rapidly obtained through minutes-long microindentation that greatly shortens the testing time.

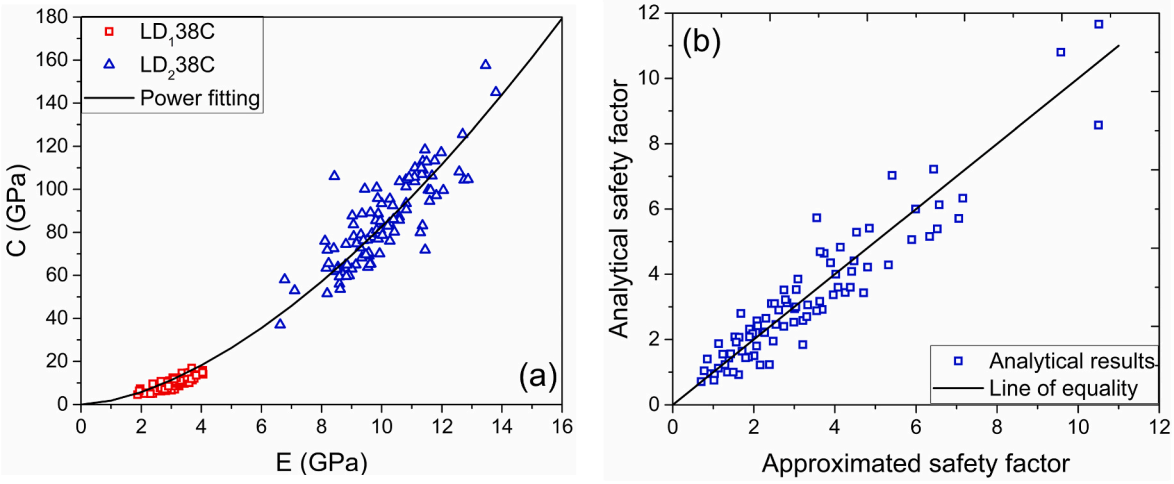

Fig. 15. (a) Found correlation between the creep modulus C and Young's modulus E for studied OWC systems ($R^2 = 0.96$); (b) correlation between the analytical safety factor and the approximated safety factor.

- The radial and tangential stress of the cement sheath both relaxed in the long term. The stress of the formation exhibited similar relaxation to the cement sheath. This confirms that the high creep of LD-OWC may be beneficial for sheath integrity.
- The long-term stress redistribution of the sheath structure showed that there was an obvious increase in the tangential stress of the steel casing shifted from the cement sheath and the formation, especially for the lower slurry density OWC. The lower the slurry density of OWC, the lower the risk of radial cracking.
- There is a power-function relationship between the safety factor of radial cracking and the key mechanical properties of LD-OWC and sheath geometrical properties. The safety factor can be employed as a first-order susceptibility index of radial cracking to compare different types of OWC materials.

Future work considering the chemical effect of aging on the elastic and creep properties is called for evaluating the durability of the cement sheath at early ages. For certain types of viscoelastic formations such as salt rock, the interaction between the cement sheath and the specific formation needs to be intensively studied.

Declaration of competing interest

The authors declare that they have no known competing financial interests or personal relationships that could have appeared to influence the work reported in this paper.

Data availability

Data will be made available on request.

Acknowledgments

The Natural Sciences and Engineering Research Council of Canada (Grant CRDPJ 485320-15) is kindly acknowledged for providing the funding for this research. We also express thanks to Nikolaos Vlasopoulos and Catherine Bouillon from Holcim company for their support and preparation of the oil well cement materials employed in this research.

Appendix A

According to the literature data of various cement systems, De Andrade and Sangesland (2016) analyzed the empirical correlation between the uniaxial compressive strength (*UCS*) and *E*, and the correlation between the tensile strength *TS* and *E*, which were written as

$$UCS = 0.00354E^2 + 3.1509E + 4.0642 \tag{A.1}$$

$$TS = 0.1502UCS - 0.5732 \tag{A.2}$$

Combining Eqs. (A.1) and (A.2), the tensile strength *TS* can be expressed in function of *E* by

$$TS = 0.0053E^2 + 0.47E \tag{A.3}$$

Eq. (A.3) can then be fitted and rewritten as a power function $TS = 0.42E^{1.1}$ for the range of Young's modulus *E* between 0.5 GPa and 16.6 GPa with $R^2 = 0.999$.

References

Abate, J., Whitt, W., 2006. A unified framework for numerically inverting Laplace transforms. Inf. J. Comput. 18, 408–421.
Alizadeh, R., Beaudoin, J.J., Raki, L., 2010. Viscoelastic nature of calcium silicate hydrate. Cem. Concr. Compos. 32, 369–376.
Ardakani, S.M., Ulm, F.-J., 2014. Chemoelastic fracture mechanics model for cement sheath integrity. J. Eng. Mech. 140, 04013009.
Bazant, Z.P., Hauggaard, A.B., Baweja, S., Ulm, F.-J., 1997. Microprestress-solidification theory for concrete creep. Aging Dry. Eff. J Eng Mech 123, 1188–1194.
Bazant, Z.P., Hubler, M.H., Yu, Q., 2011. Pervasiveness of excessive segmental bridge deflections: wake-up call for creep. ACI Struct. J. 108, 766.
Brandão, N.B., Roehl, D., de Andrade Silva, F., e Silva, R.R., 2017. The impact of cement slurry aging creep on the construction process of oil wells. J. Pet. Sci. Eng. 157, 422–429.
Brooks, J.J., Neville, A.M., 1978. Predicting long-term creep and shrinkage from short-term tests. Mag. Concr. Res. 30, 51–61.
Chen, J.J., Sorelli, L., Vandamme, M., Ulm, F.-J., Chanvillard, G., 2010. A Coupled nanoindentation/SEM-EDS study on low water/cement ratio Portland cement paste: evidence for C–S–H/Ca (OH) 2 nanocomposites. J. Am. Ceram. Soc. 93, 1484–1493.
Chen, Z., Frech-Baronet, J., Sorelli, L., 2020. Microindentation two-fold creep model for characterizing short-and long-term creep behavior of cement pastes. Mech. Mater. 103559.
Chen, Z., Sorelli, L., 2021. Effect of relative humidity and porosity on the logarithmic creep of the layered C–S–H minerals tobermorite and jennite. Cem. Concr. Compos. 103872.
Chen, Z., Sorelli, L., Frech-Baronet, J., Sanahuja, J., Vandamme, M., Chen, J., 2017. Duality between creep and relaxation of a cement paste at different levels of relative humidity: characterization by microindentation and analytical modeling. J. Nanomechanics Micromechanics 7, 04017017.
Cheng, X.W., Khorami, M., Shi, Y., Liu, K.Q., Guo, X.Y., Austin, S., Saidani, M., 2018. A new approach to improve mechanical properties and durability of low-density oil well cement composite reinforced by cellulose fibres in microstructural scale. Construct. Build. Mater. 177, 499–510.
Constantinides, G., Ulm, F.-J., 2007. The nanogranular nature of C–S–H. J. Mech. Phys. Solid. 55, 64–90.
Davies, R.J., Almond, S., Ward, R.S., Jackson, R.B., Adams, C., Worrall, F., Herringshaw, L.G., Gluyas, J.G., Whitehead, M.A., 2014. Oil and gas wells and their integrity: implications for shale and unconventional resource exploitation. Mar. Petrol. Geol. 56, 239–254.
De Andrade, J., Sangesland, S., 2016. Cement sheath failure mechanisms: numerical estimates to design for long-term well integrity. J. Pet. Sci. Eng. 147, 682–698.
Dong, X., Duan, Z., Qu, Z., Gao, D., 2019. Failure analysis for the cement with radial cracking in HPHT wells based on stress intensity factors. J. Pet. Sci. Eng. 179, 558–564.
Frech-Baronet, J., Sorelli, L., Charron, J.-P., 2017. New evidences on the effect of the internal relative humidity on the creep and relaxation behaviour of a cement paste by micro-indentation techniques. Cement Concr. Res. 91, 39–51.
Gholami, R., Aadnoy, B., Fakhari, N., 2016. A thermo-poroelastic analytical approach to evaluate cement sheath integrity in deep vertical wells. J. Pet. Sci. Eng. 147, 536–546.
Guner, D., Ozturk, H., Erkayaoglu, M., 2017. Investigation of the elastic material properties of Class G cement. Struct. Concr. 18, 84–91.
Honglin, X., Zhang, Z., Shi, T., Xiong, J., 2015. Influence of the WHCP on cement sheath stress and integrity in HTHP gas well. J. Pet. Sci. Eng. 126, 174–180.
Jennings, H.M., 2008. Refinements to colloid model of CSH in cement: CM-II. Cement Concr. Res. 38, 275–289.
Jennings, H.M., 2004. Colloid model of C– S– H and implications to the problem of creep and shrinkage. Mater. Struct. 37, 59–70.
Krakowiak, K.J., Wilson, W., James, S., Musso, S., Ulm, F.-J., 2015. Inference of the phase-to-mechanical property link via coupled X-ray spectrometry and indentation analysis: application to cement-based materials. Cement Concr. Res. 67, 271–285.
Lee, E.H., Radok, J.R.M., 1960. The Contact Problem for Viscoelastic Bodies.
Mehta, P.K., Monteiro, P.J., 2006. Concrete: Microstructure, Properties, and Materials, third ed. McGraw-Hill, New York, USA.
Nelson, E.B., 1990. Well Cementing, first ed. Elsevier, Amsterdam, Netherlands.
Neville, A.M., Dilger, W.H., Brooks, J.J., 1983. Creep of Plain and Structural Concrete, first ed. Construction press, London.

Nguyen, D.-T., Alizadeh, R., Beaudoin, J.J., Pourbeik, P., Raki, L., 2014. Microindentation creep of monophasic calcium–silicate–hydrates. Cem. Concr. Compos. 48, 118–126.
Oliver, W.C., Pharr, G.M., 2004. Measurement of hardness and elastic modulus by instrumented indentation: advances in understanding and refinements to methodology. J. Mater. Res. 19, 3–20.
Oliver, W.C., Pharr, G.M., 1992. An improved technique for determining hardness and elastic modulus using load and displacement sensing indentation experiments. J. Mater. Res. 7, 1564–1583.
Petersen, T.A., Ulm, F.-J., 2016. Radial fracture in a three-phase composite: application to wellbore cement liners at early ages. Eng. Fract. Mech. 154, 272–287.
Pichler, B., Hellmich, C., 2011. Upscaling quasi-brittle strength of cement paste and mortar: a multi-scale engineering mechanics model. Cement Concr. Res. 41, 467–476.
Sanahuja, J., Dormieux, L., 2010. Creep of a CSH gel: a micromechanical approach. An. Acad. Bras. Ciênc. 82, 25–41.
Scrivener, K., Snellings, R., Lothenbach, B., 2016. A Practical Guide to Microstructural Analysis of Cementitious Materials, first ed. Crc Press, Boca Raton, FL, USA.
Sha, F., Li, S., Liu, R., Li, Z., Zhang, Q., 2018. Experimental study on performance of cement-based grouts admixed with fly ash, bentonite, superplasticizer and water glass. Construct. Build. Mater. 161, 282–291.
Sorelli, L., Constantinides, G., Ulm, F.-J., Toutlemonde, F., 2008. The nano-mechanical signature of ultra high performance concrete by statistical nanoindentation techniques. Cement Concr. Res. 38, 1447–1456.
Sorelli, L.G., Meda, A., Plizzari, G.A., 2006. Steel fiber concrete slabs on ground: a structural matter. ACI Mater. J. 103, 551.
Tabor, D., 2000. The Hardness of Metals, first ed. Oxford university press, UK.
Taylor, H.F.W., 1997. Cement Chemistry, second ed. Thomas Telford, London, UK.
Timoshenko, S., Goodier, J.N., 1951. Theory of Elasticity, second ed. McGraw-Hill, New York, USA.
Torrenti, J.M., Benboudjema, F., Barré, F., Gallitre, E., 2014. On the very long term delayed behaviour of concrete. In: 1st International Conference on Ageing of Materials and Structures, p. 218885. Delft, Netherlands, 218885.
Torrenti, J.M., Le Roy, R., 2015. Analysis and modelling of basic creep. CONCREEP 10, 1400–1409.
Ulm, F.J., Abuhaikal, M., Petersen, T., Pellenq, R.J.M., 2014. Poro-chemo-fracture-mechanics… bottom-up: application to risk of fracture design of oil and gas cement sheath at early ages. In: Computational Modelling of Concrete Structures. CRC Press, pp. 61–71.
Valenza II, J.J., Thomas, J.J., 2012. Permeability and elastic modulus of cement paste as a function of curing temperature. Cement Concr. Res. 42, 440–446.
Vandamme, M., Ulm, F.-J., 2013. Nanoindentation investigation of creep properties of calcium silicate hydrates. Cement Concr. Res. 52, 38–52.
Vandamme, M., Ulm, F.-J., 2009. Nanogranular origin of concrete creep. Proc. Natl. Acad. Sci. USA 106, 10552–10557.
Vu, M.-H., Sulem, J., Ghabezloo, S., Laudet, J.-B., Garnier, A., Guédon, S., 2012a. Time-dependent behaviour of hardened cement paste under isotropic loading. Cement Concr. Res. 42, 789–797.
Vu, M.-H., Sulem, J., Laudet, J.-B., 2012b. Effect of the curing temperature on the creep of a hardened cement paste. Cement Concr. Res. 42, 1233–1241.
Wang, W., Taleghani, A.D., 2014. Three-dimensional analysis of cement sheath integrity around Wellbores. J. Pet. Sci. Eng. 121, 38–51.
Wang, X., Qu, Z., Dou, Y., Ma, W., 2015. Loads of casing and cement sheath in the compressive viscoelastic salt rock. J. Pet. Sci. Eng. 135, 146–151.
Wu, Y., Patel, H., Salehi, S., Mokhtari, M., 2020. Experimental and finite element modelling evaluation of cement integrity under diametric compression. J. Pet. Sci. Eng. 188, 106844.
Xi, Y., Li, J., Tao, Q., Guo, B., Liu, G., 2020. Experimental and numerical investigations of accumulated plastic deformation in cement sheath during multistage fracturing in shale gas wells. J. Pet. Sci. Eng. 187, 106790.
Yan, Y., Guan, Z., Yan, W., Wang, H., 2020. Mechanical response and damage mechanism of cement sheath during perforation in oil and gas well. J. Pet. Sci. Eng. 188, 106924.
Zhang, Q., Le Roy, R., Vandamme, M., Zuber, B., 2014. Long-term creep properties of cementitious materials: comparing microindentation testing with macroscopic uniaxial compressive testing. Cement Concr. Res. 58, 89–98.